



Cite this: *Lab Chip*, 2019, 19, 1305

Array based real-time measurement of fluid viscosities and mass-densities to monitor biological filament formation†

Paolo Oliva, ^{*,a} Benjamin Andreas Bircher,^{‡,a}
 Cora-Ann Schoenenberger^b and Thomas Braun^a

Liquid mass density and viscosity are fundamental characteristics of fluids. Their quantification by means of classical viscosity and density meters has several drawbacks: (i) the liquid-density and the viscosity cannot be measured simultaneously, (ii) sample volumes in the mL-range are consumed, (iii) the measurements cannot be multiplexed, and, (iv) the quantifications are time-consuming (minutes). Nano-mechanical transducers promise to overcome these limitations. We use fully clamped, gold coated silicon-nitride membranes with a thickness of 200 nm to measure liquid viscosity and density of samples of 1 μ L volumes residing above the membrane in a miniature well. Photo-thermal actuation is used to excite the membrane, and an optical deflection system measures the response. From the response spectra, the eigenfrequency (f) and the quality (Q) factor are extracted and used to determine liquid density and viscosity by applying a three-point calibrated, simplified lumped model. We tested the system using calibrated solutions with viscosities in the range of 1–219 mPa s and mass densities between 998 kg m⁻³ and 1235 kg m⁻³. Real-time measurements were performed that characterize the polymerization of G-actin to F-actin filaments. The method presented promises to overcome the aforementioned limitations and thereby enables the real-time characterization of sub- μ L sample volumes in a multiplexed manner.

Received 10th December 2018,
 Accepted 3rd March 2019

DOI: 10.1039/c8lc01343h

rscl.li/loc

1 Introduction

Viscosity and mass density are fundamental liquid properties. They can be measured using classical methods, *e.g.*, by employing Ostwald viscometers to measure the fluid viscosity or by the application of volume-measuring containers in combination with mass balances to determine the liquid density. However, these conventional methods need milliliter sample volumes, and the measurement takes a significant amount of time.

Over the past few years, several methods have been proposed to minimize sample volumes and reduce measurement times. These can be classified as miniaturized Ostwald viscometers employing microfluidics technology,¹ droplet-based microfluidics methods,² thermal noise detection,³ and thickness-shear resonators (QCM or SH-SAW sensors).^{4,5} A broad research domain is based on the development of micro-rheology assays,

which are used to measure rheological properties of a medium, such as the viscoelasticity and the loss and shear modulus of biological filaments, at small scales. These new techniques include dynamic light scattering (DLS),⁶ diffuse wave spectroscopy (DWS),^{7,8} video-particle tracking,⁹ microfluidic stagnation flow,^{10–12} and microfluidic capillary viscometry.^{13–18}

Cantilever-based nano-mechanical sensors allow the real-time measurement of liquid mass-density and viscosity of μ L-sized volumes.^{19,20} These sensors characterize the cantilever vibrational response to external driving forces. Excitation can be achieved in different ways: photo-thermally,^{21–23} by inducing Lorentz forces,^{24,25} and piezo-electrically.^{26,27} For example, cantilevers were used as sensors to measure the coagulation of blood plasma.^{28,29}

However, these cantilever-based sensors have limitations: First, the strong damping of fully-immersed cantilevers leads to low-quality factors (Q) and, thus, limits measurement precision and prevents the characterization of liquids with high viscosities. Second, non-transparent liquids disturb the optical readout system that measures the deflection of the cantilever. Third, multiplexed real-time measurements are difficult because either an array of cantilevers measures geometrically-separated liquid droplets, or a stream of sequential liquid droplets passes the cantilever transducer. The latter allows high-throughput screening, but individual samples are

^a Center for Cellular Imaging and Nanoanalytics (C-CINA), University of Basel, Mattenstrasse 26, Basel, Switzerland. E-mail: paolo.oliva@unibas.ch, thomas.braun@unibas.ch

^b Department of Chemistry, University of Basel, Mattenstrasse 24a, Basel, Switzerland. E-mail: cora-ann.schoenenberger@unibas.ch

† Electronic supplementary information (ESI) available. See DOI: 10.1039/c8lc01343h

‡ Current address: Federal Institute of Metrology, Lindenweg 50, Bern-Wabern, Switzerland E-mail: benjamin.bircher@metas.ch.



exposed only for a short period of approximately 1 s^{20} which is usually too short to allow rheokinetic measurements of chemical reactions.¹⁹

In this report, we use fully clamped silicon-nitride membranes, that are photo-thermally excited, in combination with an optical read-out system that enables the recording of spurious-free response-spectra of the membrane. From the response spectra the eigenfrequency (f) and the quality factor (Q) were extracted by using the driven damped harmonic oscillator model (DDHO) (ch. 2†). The extracted values were subsequently used to determine the liquid density and viscosity by applying the reduced order model (ROM),³⁰ which is based on a three-point calibration. This system has several advantages: (i) the membrane and the silicon base form a tiny well, and only sub-microliter sample volumes are needed, (ii) higher viscosity and mass density resolution is achieved due to higher Q -factors,³¹ (iii) the membranes can be arrayed for multiplexed measurements, and, (iv) broad measurable liquid density and viscosity range.

2 Materials and methods

2.1 Reference solutions

Reference solutions were prepared by mixing liquid glycerine (Cat-nr. 131339.1211, PanRec AppliChem, ITW Reagents) with water for molecular biology (Cat-nr. H20MB0501, Millipore). The reference viscosities and mass densities were measured with an automated viscosity (Anton Paar, AMVn Viscometer, Switzerland) and density meter (Anton Paar, DMA 4500, Switzerland). For details see ESI,† ch. 1.

2.2 Protein solutions

Lyophilized G-actin (globular actin) from rabbit skeletal muscle (Cat-nr. 8101-01), G-actin buffer at pH 8.2, containing adenosinetriphosphate (ATP), CaCl_2 and dithiothreitol (DTT) (MonoMix, Cat-nr. 5100-01) and polymerization inducing buffer PolyMix (Cat-nr. 5000-01) were purchased from Hypermol (Bielefeld, Germany). Before the experiments the G-actin lyophilized powder was reconstituted with water to a final concentration of 1 mg mL^{-1} , centrifuged for 10 min ($15\,000 \times g$) and stored on ice.

2.3 Sensor setup

Fig. 1 shows the membrane transducer, the liquid handling system, and its integration in the set-up. Fig. 2 depicts a schematic representation of the photo-thermal excitation, the optical beam deflection system (OBD), and the electronic components adapted from a previous setup.²⁰ These components enable the use of silicon-nitride membranes as nano-mechanical resonators.

The set-up consists of a detection- and an excitation part, which are mechanically separated from the measurement chamber. The detection part is composed of a laser beam (LD_{DE} , $\lambda = 785.4\text{ nm}$, $P_{\text{DE}} = 4.9\text{ mW}$; 51nanoFCM-H06, Schäfer + Kirchhoff GmbH, Hamburg, Germany) with a wavelength of

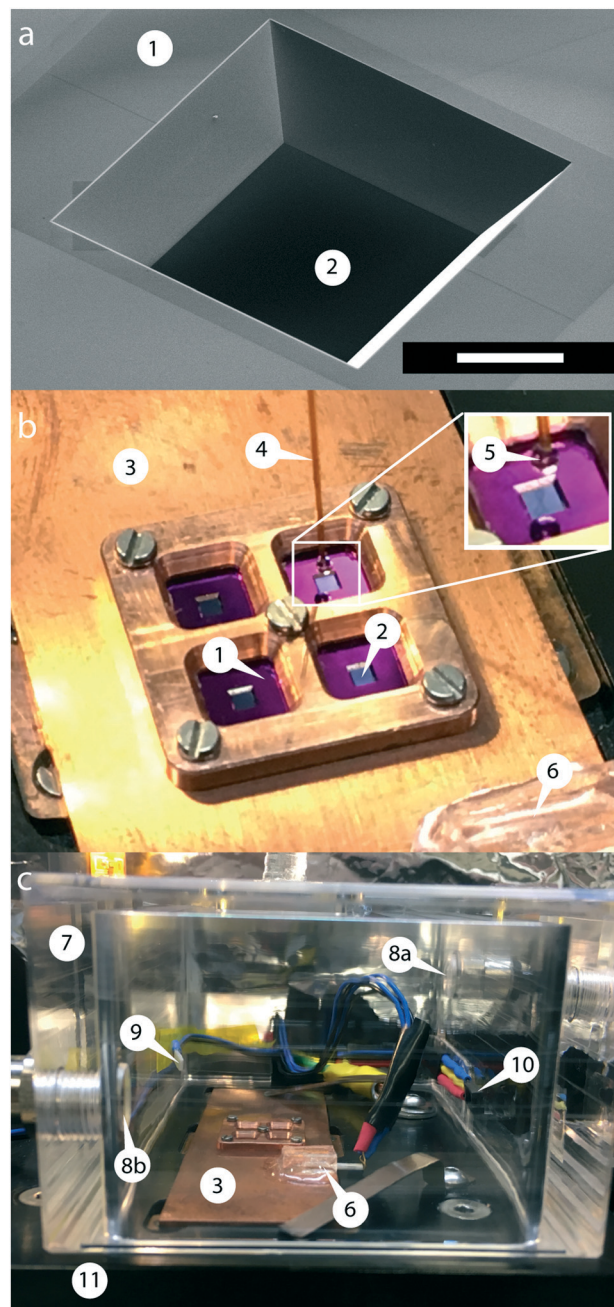


Fig. 1 Membrane transducer, liquid handling system and environment control. (a) SEM-image of a typical membrane transducer: the silicon-frame (1) and the silicon-nitride membrane (2) form a well (frame size: $5 \times 5\text{ mm}^2$, window size: $1 \times 1\text{ mm}^2$, thickness: 200 nm), which can be filled with the test liquid. The stoichiometric membrane windows are made of Si_3N_4 -films with a high tensile stress (1 GPa). The 54.74° angle is defined by the silicon (111)-plane. Scale bar: $400\text{ }\mu\text{m}$. (b) Mounting of nano-mechanical membranes and sample priming: (3) temperature-controlled copper plate; (4) fused silica capillary for sample deposition on the silicon-nitride membrane; (5) sample droplet; (6) temperature sensor used to regulate the temperature of the membrane holder; (1) silicon frame with (2) silicon-nitride membrane. Inset: Silicon-nitride membrane with sample priming; (c) temperature and humidity controlled chamber mounted on a XY-stage; (7) humidity chamber made of plexiglass; (8a) inlet and (8b) outlet of humid air; (9) temperature sensor monitoring the temperature of the humidity chamber; (10) humidity sensor monitoring the relative humidity inside the chamber; (11) XY-stage.





Fig. 2 Schematic view of the electronics and optical components. Optical beam deflection (red line) is used to detect the oscillations of the silicon-nitride membrane. A laser beam (LD_{DE}) with a wavelength of 785.4 nm sequentially passes a collimator (COL1), a polarizing beam-splitter (PBS) and quarter-wave plate (QWP). To align the detection-laser placement on the membrane, we inserted a dielectric broadband mirror (DBM1). The excitation part of the setup (blue line) consists of a laser beam (LD_{EX}) with a wavelength of 405 nm passing through a collimator (COL2), a dielectric broadband mirror (DBM2) and a dichroic mirror (DM). Both laser beams are reflected by a broadband mirror (BM1) and focused onto the membrane by a microscope objective (OBJ, 4 \times). The excitation laser is driven by a variable frequency oscillator (VFO), and a lock-in amplifier (LIA) detects the response amplitude; both electronic components are integrated within the ZI-HF2LI (Zurich Instruments). The reflected beam passes through two broadband mirrors (BM) and is finally detected by a quadrant photo-diode (QPD). To optimize the detection of a specific wavelength an optical filter (OF) is mounted in front of the QPD.

785.4 nm which sequentially passes through a collimator (COL1; TC12APC-780, Thorlabs, Germany) and an optical isolator (ISO; IO-3D-780-VLP, Thorlabs, Germany). For monitoring the intensity of the detection laser, a beam-splitter (8:92; CM1-BP108, Thorlabs, Germany) with a photo-diode (PD1; PDA100A-EC, Thorlabs, Germany) has been mounted after the optical isolator. To obtain circularly polarized light, a polarizing beam-splitter (PBS; CM1-PBS252, Thorlabs, Germany) and a quarter wave-plate (QWP; AQWP05M-600, Thorlabs, Germany) have been inserted in the optical pathway. The laser beam finally reflects at a broadband mirror (BM1; BB1-EO2, Thorlabs, Germany) and is focused using a microscope objective (OBJ; RMS4X, Thorlabs, Germany). The beam reflects off the gold-coated surface of the silicon nitride membrane and follows the same optical pathway ending on a quadrant photodiode (QPD; S5980, Hamamatsu, Japan), which is placed after the PBS. The newly designed QPD has a bandwidth of 3.5 MHz.

The excitation part of the setup is composed of a laser beam (LD_{EX} , $\lambda = 405$ nm, $P_{EX} = 8.7$ mW; DLM-405/70F, Elovivis)

with a wavelength of 405 nm, which passes through a collimator (COL2; TC12FC-405, Thorlabs, Germany), a beam-splitter (8:92; CM1-BP108, Thorlabs, Germany), a dichroic mirror (DM; DMLP567, Thorlabs, Germany), and a broadband mirror (BM1), and is finally focused on the gold-coated membrane using the same objective (OBJ).

Using the internal variable frequency oscillator (VFO) and lock-in amplifier (LIA) integrated with Zurich Instruments HF2LI (ZI-HF2LI), the amplitude and phase spectra of different modes were recorded. The reference signal is fed into the excitation laser which drives the oscillation of the membrane. To monitor the dynamic deflection detected by the QPD, the input signal was split into two components: the first line was used as an input signal to the Zurich Instruments lock-in amplifier. The QPD used was designed to reach a 10-fold amplification. The second line was first low-pass filtered ($f_{c,DC} = 80$ Hz) and then amplified ten times, to avoid noise amplification. This component was then fed into an analog input of a National Instruments card (NI-9215) and read out.

The new control software was developed as an openBEB module³² in LabVIEW. To collect and save the amplitude and phase data, a separate module was programmed, which enables the user to perform either a single sweep or a sequential acquisition of a specific frequency range.

2.4 Data analysis collection

Fig. 3 shows a schematic representation of a typical measurement. To measure the liquid density and the viscosity, the quality factor and the eigenfrequency were tracked by sweeping the modulation frequency of the excitation laser and recording the frequency-dependent response of the membrane using the read-out laser. From a series of response-spectra, the eigenfrequency and the quality factor were determined. The reduced order model³⁰ enables the determination of the liquid viscosity and density after a three-point calibration³⁰ (ch. 2†). By measuring the eigenfrequencies (f_{exp}) and the quality factors (Q_{exp}) of three known liquids which cover a broad density and viscosity range, the calibration coefficients,

m_{0k} , m_{pk} , $m_{\eta pk}^*$, c_{0k} , $c_{\eta k}$, $c_{\eta pk}^*$, of the reduced order model can be determined. The resulting values are inserted into the following equations and solved for the liquid density, ρ , and the viscosity η :

$$f_{exp} \approx \frac{1}{2\pi \sqrt{m_{0k} + m_{pk} \times \rho + m_{\eta pk}^* \times \sqrt{\eta \rho}}}, \quad (1)$$

$$Q_{exp} \approx \frac{\sqrt{m_{0k} + m_{pk} \times \rho + m_{\eta pk}^* \times \sqrt{\eta \rho}}}{c_{0k} + c_{\eta k} \times \eta + c_{\eta pk}^* \times \sqrt{\eta \rho}} \quad (2)$$

Before starting with the measurements, the detection and excitation laser were aligned. The laser positioning on the silicon-nitride membrane is simplified by calculating the Jacobi- and Hess matrix of the respective mode shape



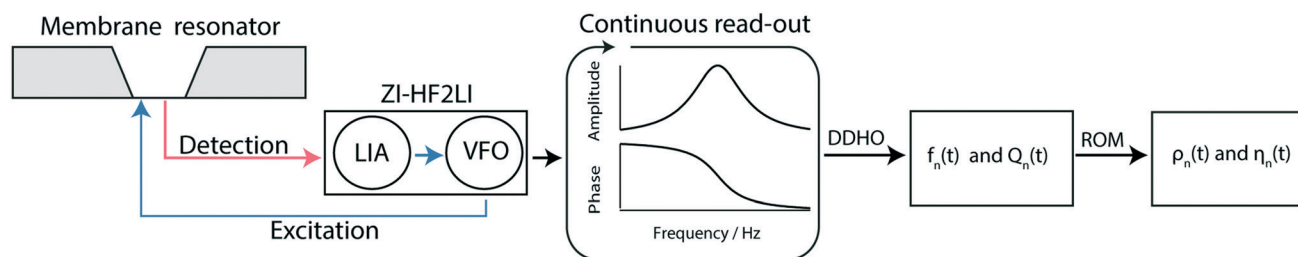


Fig. 3 Schematic overview of the measurement workflow: the membrane resonator is actuated by a modulated laser diode (blue) driven by the variable frequency oscillator (VFO). The membrane response is optically read out (red laser) and quantified by a digital lock-in amplifier (LIA). Note that the gold layer on the membrane absorbs 67% of the incoming blue light leading to a photo-thermal actuation of the membrane, and reflects 97% of the red light for the read-out of the membrane response.¹⁹ Spectra are recorded continuously by sweeping the frequency space, resulting in a time series of amplitude and phase spectra. From the series of amplitude and phase response spectra, the time-dependent eigenfrequency $f_n(t)$ and the time-dependent quality factors $Q_n(t)$ can be determined by fitting a driven damped harmonic oscillator model (DDHO) to each spectrum. After the determination of these parameters the liquid density $\rho_n(t)$ and the viscosity $\eta_n(t)$ can be calculated by applying the reduced order model (ROM).³⁰

function. It is essential to determine the correct placement of the excitation and detection otherwise the vibrational amplitudes are strongly reduced.²³

After having placed the laser spots on a distinct area, the spectrum of a reference fluid was determined by a sweep over a frequency range (from 5 kHz to 200 kHz). Next, the vibrational mode was chosen. By choosing modes with higher eigenfrequencies, the sensitivity to viscosity and mass density changes is increased.³³ Because of the higher amplitude and the highest signal-to-noise ratio, we typically chose the second peak around 35.8 kHz for our experiments (see Fig. 4). The mode shapes represent the superposition of lower modes.³⁴

After having selected the mode, the respective frequency range was chosen and again swept repeatedly. The resulting amplitude and phase curves were analyzed in the following ways: (i) Lorentzian fit to the amplitude, (ii) peak frequency and quality factor were extracted, and, (iii) the phase curve was fitted by a driven damped harmonic oscillator model (DDHO) using the derived parameters from the Lorentzian as starting points (ch. 5†).

2.5 Humidity chamber, sample stage, and sample priming

To avoid thermal and ambient-induced deflection drifts,³⁵ viscosity changes, and evaporation of the sample the environment was controlled by placing the membrane transducer in a specially designed climate chamber made of plexiglass (Fig. 1c). The humidity of the chamber was regulated at 73% for a dew-point temperature of 20 °C, and all experiments were performed at this temperature.

To regulate the humidity set-point, a humidity sensor (HIH-4000-002, Honeywell, Distrelec, Switzerland) was installed. The humid air is introduced from an MH-Series humidifier (MH-110-12S-2, Perma Pure, New Jersey, USA) which contains a selectively permeable Nafion membrane surrounded by water. After passing the walls of this membrane the water evaporates due to the pressure difference

between the incoming dry gas and the water supply. This humidifying tube allows the transfer of heat and water vapor pressure between a gas stream and a water supply. The flow rate is controlled using a calibrated flow meter (Q140E13G, Vögtlin Instruments, Aesch, Switzerland). Typically a flow rate of 1.667 L min⁻¹ is used. To avoid cooling of the tube and therefore decreasing the humidification efficiency, a resistor wire (Block, FA-Nr. 708951, Distrelec, Switzerland) was wrapped around it. Using a PID-Controller the current through the wire can be regulated. The resistor wire has a total resistance of 100.8 Ω and with this heating system a maximum relative humidity of 90.4% at 24 °C ($T_{\text{tube}} = 27$ °C) can be achieved. The temperature of the copper plate was regulated with an accuracy of ±0.05% using two Peltier-elements and a PID-controller.

Sample volumes were typically 1 μL, which requires a precise pumping system with a minimal dead volume. A syringe pump (KDS900, KD Scientific, Holliston, MA, U.S.A.) and a 500 μL syringe were used to aspirate a few microliters of the test sample. Using a fused silica capillary (TSP-180350, ID = 180 μm, OD = 350 μm) that is connected to the syringe and mounted on a movable XYZ-stage, the sample droplet can be precisely placed on the silicon-nitride membrane. A surveillance camera (Prosilica GC750C, Basler, Germany) with a mounted 12× zoom body tube (1-50330, Navitar, USA) facilitates the alignment of the capillary (Fig. 1b).

2.6 Membrane preparation

Stoichiometric silicon-nitride membranes (NSX5100D, Norcada, Edmonton, Canada) with a window size of 1 × 1 mm² and a thickness of 200 nm spanned over a 5 × 5 mm² silicon support were used.

Before each experiment, the membranes were washed with acetone, rinsed with nanopure water, and then plasma cleaned (O₂, gas flow 0.003379 Pa m³ s⁻¹, 13.32 Pa, power 30 W; Solarus, Model 950, Gatan) for 40 s. Subsequently, 0.4 μL of a PLL(20)-g[3.5]-PEG(2) solution at a concentration of 1 mg





Fig. 4 Photo-thermal actuation of a nanomechanical membrane loaded with 1 μL of water. (a) The amplitude spectrum of the nanomechanical membrane measured under load. The spectrum was obtained by sweeping the frequency domain between 5 kHz and 200 kHz using the variable frequency oscillator to modulate the actuation laser. For the normalized amplitude-spectrum (red) a multi-peak analysis with a constant baseline (green) was performed, and the individual peaks were fitted with the damped harmonic oscillator model (black). The residual amplitudes between the model fitting and the measured values are shown below the spectrum. (b) Amplitude and phase curve of the second peak marked with an asterisk in panel (a). Measured data are shown in red, and the fitted driven damped harmonic oscillator are shown in black. (c) Simulated mode shape function of the analyzed peak. The color legend represents the normalized vibrational amplitude.

mL^{-1} (SuSoS AG, Dübendorf, Switzerland) was deposited in the well and incubated for 1 h at room temperature. After this step, the membrane was rinsed with nanopure water. The membrane passivation was done to avoid protein sticking to the silicon-nitride surface, which would cause errors in the measured fluid properties.

2.7 Finite element simulations of membrane behaviours

2.7.1 Determination of the membrane eigenmodes. To compare the measured peaks in the amplitude spectrum, a finite element simulation was performed. For this purpose two blocks of different sizes and materials were designed in COMSOL Multiphysics®. One block represents the Si_3N_4 -membrane with a window size of $1 \times 1 \text{ mm}^2$ and a thickness of 200 nm. The other one is the refractive gold substrate with a corresponding thickness of 20 nm. Material properties were adapted from the original COMSOL library.

To analyze the eigenfrequency of a fully clamped membrane the solid mechanics and heat transfer modules were used and combined with a thermal expansion multiphysics module. Due to the laser heating up the gold layer, a material-dependent expansion causes the oscillation of the membrane. The tensile stress of the silicon-nitride layer and the mass added to the well damped the oscillation. In the simulation the added mass corresponds to 1 μL of water. The physics modules were integrated in a pre-stressed eigenfrequency analysis. For the meshing the entire geometry was divided into two parts. A free triangular node with an extremely fine element size was added to the upper and lower surface of the blocks. The mesh of the remaining geometry was divided into 400 equally distributed rectangulars per domain.

2.8 Electron microscopy specimen preparation

We used transmission electron microscopy (TEM) of negatively stained samples to observe the presence (or absence) of actin filaments. After the liquid viscosity measurement, the sample was removed from the silicon-nitride well and applied to a glow-discharged carbon-coated EM-grid. The sample was adsorbed to the grid for 75 s at room temperature. Excess liquid was blotted with filter-paper, and subsequently the grid was washed for three times with 5 μL of nanopure water. After washing, the sample was negatively stained twice for 20 s with 5 μL of 2% uranyl acetate.

3 Results

3.1 Photo-thermal excitation of silicon-nitride membranes

To test the photo-thermal actuation and beam-deflection read-out system, we measured the amplitude response spectrum of the nanomechanical membrane loaded with 1 μL of water. Eight eigenfrequency peaks were observed in the amplitude spectrum (Fig. 4a). However, below 5 kHz the peak-amplitudes are close to the noise level. The found eigenfrequencies are in excellent agreement with our simulations (Table 1). Furthermore, we characterized the second peak at 35.8 kHz by sweeping over a frequency range of 5 kHz to 200 kHz as shown in Fig. 4b. The bandwidth of the variable frequency oscillator was adapted to minimize the noise; usually, a bandwidth of 15.1 Hz was used. Note, that for the subsequent measurements we used the eigenfrequency around 35.8 kHz.



silicon-nitride membranes. First, each membrane resonator was individually calibrated. As calibration fluids, diluted glycerol solutions (30% V/V, 50% V/V) and water were used. After the calibration four different fluids were placed in the well of individual membranes. The mechanical stage allowed the subsequent analysis of the individual fluids by moving the membrane onto the optical window. Fluid characterization was performed as described above, and the results are shown in Fig. 5a.

In addition to the viscosity and mass density measurements, the formation of actin filaments in real-time was tracked as follows: 0.9 μL of monomeric G-actin was placed on the silicon-nitride membrane. The excitation and detection of the membrane oscillations were started, and an equilibrium state of the eigenfrequency was obtained after 20 min. Subsequently, 0.1 μL of PolyMix at pH 7.4, containing KCl, ATP and MgCl_2 , was added to trigger actin polymerization. Immediately, the sequential acquisition of the amplitude and phase curve with a digital lock-in amplifier was started and run for 50 min (Fig. 6a). After the addition of 0.1 μL PolyMix, a slowly decreasing quality factor was observed. The eigenfrequency rapidly changed and achieved a steady-state after a few minutes (Fig. 6a). As a negative control, the same experiment was performed by adding 0.1 μL MonoMix buffer at pH 8.2 containing ATP, CaCl_2 and DTT that does not promote F-actin formation (Fig. 6b). Some fluctuations of the eigenfrequencies and quality factors were observed with the MonoMix buffer, but compared to using PolyMix, no significant decrease of the quality factor was observed (Fig. 6b): the eigenfrequency drop of approximately 0.2% is due to the addition of 0.1 μL MonoMix buffer. To confirm that the polymerization of G-actin was not dependent on the specific membrane, the entire measurement was repeated several times using different membranes (ch. 4†).

After the measurement, the droplet was collected from the membrane, negatively stained and visualized in the electron microscope. As illustrated in Fig. 7 the sample contained long actin filaments.

4.1 Photo-thermal excitation of silicon-nitride membranes

We used photo-thermal excitation of fully clamped silicon-nitride membranes that form a small well with the silicon base. Membranes with a frame size of $1 \times 1 \text{ mm}^2$ were used to perform measurements of volumes between $0.5 \text{ }\mu\text{L}$ and $1 \text{ }\mu\text{L}$. Compared to fully immersed resonators, a particular advantage of these transducers is the higher quality factor that results in a higher viscosity and mass density resolution. By analyzing the second vibrational mode, we were able to achieve a quality factor of $Q = 135$ using water loaded membranes with this set-up. In comparison cantilever-based sensors²⁰ reach a quality factor of $Q = 10$ for the third vibrational mode. However, at frequencies lower than 5 kHz the

We noticed, that the calibration fluids chosen need to cover the expected viscosity range of the test-fluids. An extrapolation of the model to viscosity measurements that were far away from the calibration liquids led to significant errors. In order to cover the large range of viscosities, we used two calibration sets: for lowly viscous fluids (from 0 mPa s to 6.63 mPa s), the chosen calibration fluids were 0%-, 30%- and 50%-glycerol (Fig. 5a). For highly viscous fluids (from 13.2 mPa s to 219 mPa s) 30%-, 60%- and 90%-glycerol were chosen as reference fluids (Fig. 5b). In both calibration sets 30%-glycerol was chosen as the calibration point in order to avoid large deviations in the calculation of the liquid properties of the test sample. For highly viscous fluids, the test sample was 85%-glycerol.

3.2.2 Multiplexed liquid viscosities and mass densities measurements. We measured the liquid viscosities and mass densities of four test-fluids in parallel using an array of four

f_{exp} [Hz]	f_{sim} [Hz]
$17\,247 \pm 64.22$	17 218
$35\,862 \pm 23.66$	35 866
$62\,488 \pm 41.73$	62 494
$76\,894 \pm 52.28$	76 895

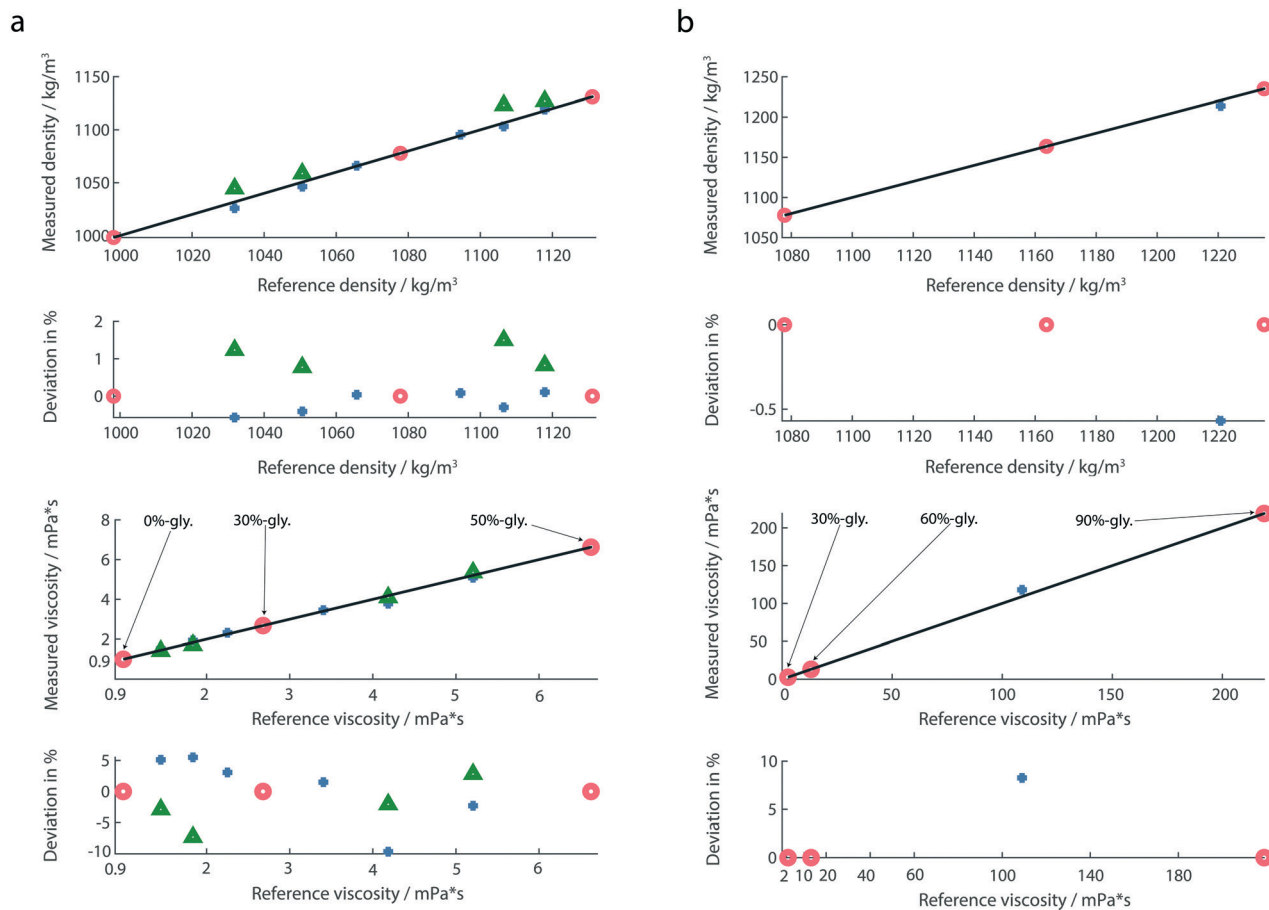


Fig. 5 (a) Mass densities and viscosities of diluted glycerol solutions and water. Water, 30%-, and 50%-glycerol solutions (red circles) were used as calibration fluids and the viscosity and mass density of the remaining liquids (blue marks) was measured. Relative deviations from the reference values are shown below. Additionally, the mass densities and viscosities of four liquids (green triangles) were measured with membranes placed in an array. (b) Calibration fluids were 30%-, 60%- and 90%-glycerol (red circles). For the highly viscous fluid (85%-glycerol) the deviations were calculated from the theoretical values due to limitations of the commercially available viscometer.

peak amplitudes were close to the noise level. The lower limit corresponds to the bandwidth of the read-out electronics. We observed an upper limit (around 60 kHz) which could be due to (i) inefficient heat transfer needed to relax the tension introduced in the membrane bilayer after the photon pulse, or (ii) the clamping loss.

Heat transfer simulations show that the cooling time of the stressed bilayer after a laser pulse is enough to induce oscillation. The so-called phonon-tunneling, which is an external loss, is one of the significant damping effects of membrane resonators. To avoid the propagation of acoustic waves into the silicon frame, the vibrational mode has to be placed within a phononic bandgap. For blocking acoustic waves a phononic crystal and the membrane frame should form a defect.

Commercially available membrane do not fulfill the above criterion. Simulation show a bandgap between 600–800 kHz indicating that the missing phononic bandgap could be responsible for the high damping effect in the low-frequency regime (ch. 6†). To achieve a higher signal-to-noise ratio (higher quality factor) and increase the bandwidth, a new silicon base could be designed. The dimensions of the new

silicon base have to be determined in such a way that a phononic bandgap is present within the wanted frequency range.

4.2 Viscosity and mass density measurements of Newtonian liquids

As indicated by maximal deviations of 1.5% for the mass density and 9.6% for the viscosity (Fig. 5a), the determination of the mass density is more accurate than that of the viscosity. Compared to previous studies,²⁰ we observed a larger deviation in the determination of the viscosity. A possible reason is the use of a different environment controlling system. A slight change in the temperature and humidity could affect the liquid properties. Another measure which could further minimize the measured deviation is the integration of an interferometer instead of an optical beam deflection read-out system.

By performing multiplexed measurements, we could further minimize the measurement time and realize a high-throughput at the same accuracy.





Fig. 6 Real-time characterization of F-actin formation. (a) Measured eigenfrequencies, quality factors and the corresponding mass densities and viscosities of polymerizing actin. The values were calculated by applying the reduced order model. Each color and each mark represents one measurement performed with the same silicon-nitride membrane. The red, black, blue and green marks represent the first, second, third, and fourth run respectively; (b) measured eigenfrequencies, quality factors and the corresponding mass densities and viscosities of actin in the absence of polymerization conditions (negative control). The eigenfrequency changes of approx. 0.2% reflects the addition of 0.1 μ L of MonoMix.



Fig. 7 Post-measurement sample analysis by transmission electron microscopy. Long actin filaments are detected in G-actin samples that were incubated with polymerization buffer. Scale bar: 100 nm.

An additional advantage of our set-up is the broad range of viscosity and mass density that can be measured (Fig. 5b). Experiments with highly viscous glycerol solutions were performed. In the case of highly viscous glycerol solutions the determination of the reference viscosities by the classical Anton Paar viscometer was not possible due to the high rolling time. Instead, the theoretical values for the viscosities of 85%- and 90%-glycerol were used.

The use of the reduced order model leads to an accurate density and viscosity determination only if the calibration fluids have the same viscosity–density behavior and range as the sample liquids. An extrapolation of the liquid properties should be avoided. Further information can be found in the ESI† (ch. 2).

4.3 Real-time characterization of G-actin polymerization

By measuring mass density and viscosity, we were able to follow G-actin polymerization in real-time in a label-free manner. In previous studies, the filament formation and



The ability to follow filament formation in real-time was also confirmed by the negative control (Fig. 6b). In the absence of polymerization inducing buffer, fluctuating eigenfrequencies and quality factors were visible, but no significant decrease or increase of the quality factor and eigenfrequency were observed over time.

We envisage that the improved measurement platform is suitable to characterize interactions of biomolecules in a label and functionalization-free manner.

T. B. conceived the research project. B. A. B. helped with the manuscript preparation and previously developed the device

- 1 M. Zou, S. Cai, Z. Zhao, L. Chen, Y. Chen, X. Fan and S. Chen, *Rev. Sci. Instrum.*, 2015, **86**, 104302.
- 2 Y. Li, K. R. Ward and M. A. Burns, *Anal. Chem.*, 2017, **89**, 3996–4006.
- 3 F. A. Sandoval, M. Sepúlveda, L. Bellon and F. Melo, *Sensors*, 2015, **15**, 27905–27916.
- 4 G. L. Hayward and G. Z. Chu, *Anal. Chim. Acta*, 1994, **288**, 179–185.
- 5 T. Morita, M. Sugimoto and J. Kondoh, *Jpn. J. Appl. Phys.*, 2009, **48**, 07GG15.
- 6 F. He, G. W. Becker, J. R. Litowski, L. O. Narhi, D. N. Brems and V. I. Razinkov, *Anal. Biochem.*, 2010, **399**, 141–143.
- 7 D. Weitz, J. Zhu, D. J. Durian, H. Gang and D. J. Pine, *Phys. Scr.*, 1993, **T49**, 610–621.
- 8 T. Mason, H. Gang and D. A. Woltz, *J. Opt. Soc. Am. A*, 1997, **14**, 139–149.
- 9 F. Ortega, H. Ritacco and R. G. Rubio, *Curr. Opin. Colloid Interface Sci.*, 2010, **15**, 237–245.
- 10 G. G. Fuller and L. G. Leal, *Rheol. Acta*, 1980, **19**, 580–600.
- 11 J. F. Schoonen, F. H. Swartjes, G. W. Peters, F. Baaijens and H. E. Meijer, *J. Non-Newtonian Fluid Mech.*, 1998, **79**, 529–561.
- 12 S. D. Hudson, F. R. Phelan, M. D. Handler, J. T. Cabral, K. B. Migler and E. J. Amis, *Appl. Phys. Lett.*, 2004, **85**, 335–337.
- 13 K. Kang, L. J. Lee and K. W. Koelling, *Exp. Fluids*, 2005, **38**, 222–232.

- 14 C. J. Pipe, T. S. Majmudar and G. H. McKinley, *Rheol. Acta*, 2008, **47**, 621–642.
- 15 N. Srivastava, R. D. Davenport and M. A. Burns, *Anal. Chem.*, 2005, **77**, 383–392.
- 16 G. Degré, P. Joseph, P. Tabeling, S. Lerouge, M. Cloitre and A. Ajdari, *Appl. Phys. Lett.*, 2006, **89**, 24104.
- 17 Z. Han, X. Tang and B. Zheng, *J. Micromech. Microeng.*, 2007, **17**, 1828–1834.
- 18 Y.-Y. Lin, C.-W. Lin, L.-J. Yang and A.-B. Wang, *Electrochim. Acta*, 2007, **52**, 2876–2883.
- 19 B. A. Bircher, L. Duempelmann, K. Renggli, H. P. Lang, C. Gerber, N. Bruns and T. Braun, *Anal. Chem.*, 2013, **85**, 8676–8683.
- 20 B. A. Bircher, R. Krenger and T. Braun, *Sens. Actuators, B*, 2016, **223**, 784–790.
- 21 D. Ramos, J. Tamayo, J. Mertens and M. Calleja, *J. Appl. Phys.*, 2006, **99**, 124904.
- 22 D. Ramos, J. Mertens, M. Calleja and J. Tamayo, *Appl. Phys. Lett.*, 2008, **92**, 173108.
- 23 B. A. Bircher, H. P. Lang, L. Duempelmann, C. Gerber and T. Braun, *Micro Nano Lett.*, 2013, **8**, 770–774.
- 24 O. Enders, F. Korte and H.-A. Kolb, *Surf. Interface Anal.*, 2004, **36**, 119–123.
- 25 S. Somnath, J. O. Liu, M. Bakir, C. B. Prater and W. P. King, *Nanotechnology*, 2014, **25**, 395501.
- 26 H. Asakawa and T. Fukuma, *Rev. Sci. Instrum.*, 2009, **80**, 103703.
- 27 S. S. Lee and R. M. White, *Sens. Actuators, A*, 1996, **52**, 41–45.
- 28 O. Cakmak, C. Elbuken, E. Ermek, A. Mostafazadeh, I. Baris, B. E. Alaca, I. H. Kavakli and H. Urey, *Methods*, 2013, **63**, 225–232.
- 29 F. Padovani, J. Duffy and M. Hegner, *Anal. Chem.*, 2017, **89**, 751–758.
- 30 M. Heinisch, E. K. Reichel, I. Dufour and B. Jakoby, *Procedia Eng.*, 2014, **87**, 472–475.
- 31 Z. Wu and X. Ma, *Proc. R. Soc. A*, 2016, **472**, 20150728.
- 32 C. Ramakrishnan, A. Bieri, N. Sauter, S. Roizard, P. Ringler, S. A. Mueller, K. N. Goldie, K. Enimanev, H. Stahlberg, B. Rinn and T. Braun, *BMC Bioinf.*, 2014, **15**, 84.
- 33 M. K. Ghatkesar, V. Barwich, T. Braun, J.-P. Ramseyer, C. Gerber, M. Hegner, H. P. Lang, U. Drechsler and M. Despont, *Nanotechnology*, 2007, **18**, 445502.
- 34 F. Duvinneau, S. Koch, R. Orszulik, E. Woschke and U. Gabbert, *Technische Mechanik*, 2016, **36**, 180–189.
- 35 T. Thundat, R. J. Warmack, G. Y. Chen and D. P. Allison, *Appl. Phys. Lett.*, 1994, **64**, 2894–2896.
- 36 N. Strelnikova, F. Herren, C.-A. Schoenenberger and T. Pfohl, *Front. Mater.*, 2016, **3**, 2707.
- 37 P. Rust, I. Leibacher and J. Dual, *Procedia Eng.*, 2011, **25**, 587–590.

